

# Numerical simulation of the equilibrium and transport of a centrifugally confined plasma

B. R. Osborn, R. F. Ellis, and A. B. Hassam

*Institute for Plasma Research, University of Maryland, College Park, Maryland 20742*

(Received 13 August 2002; accepted 7 March 2003)

A centrifugally confined plasma utilizes centrifugal forces from supersonic plasma rotation to augment the conventional magnetic confinement of fusion plasmas. Appropriately used, plasma pressure can be contained along the magnetic field lines, allowing for “open” configurations, introducing flexibility in design. The axisymmetric equilibrium of one such system, a single coil configuration, is investigated numerically. Plasma “detachment” is shown at Mach numbers ranging from 3 to 4. It is also shown how flow shear heats the plasma by viscous dissipation. Profiles relaxed with respect to plasma transport are shown. © 2003 American Institute of Physics.

[DOI: 10.1063/1.1571543]

## I. INTRODUCTION

Centrifugal confinement is based on the idea that centrifugal forces from supersonic plasma rotation can be used, in conjunction with magnetic confinement, to effect confinement of plasmas along the magnetic field.<sup>1,2</sup> Configurations that could be used for thermonuclear fusion plasmas can be found. The simplest case<sup>1</sup> is schematically described by Fig. 1. A toroidal coil carries a current that produces a poloidal, axisymmetric dipolar magnetic field. The coil is supported by a brace extending from the inner wall. An insulator electrically isolates the brace from the vacuum vessel. Leads from the central core maintain the coil current. In addition, the coil is maintained at high voltage with respect to the vessel. The coil–vessel system is thus a capacitor. A plasma placed in the vessel spins toroidally from the resulting  $\mathbf{E} \times \mathbf{B}$  drift. If this rotational speed is high enough, the radially outward centrifugal force will keep the plasma on the outboard side of the magnetic field surfaces, thus isolating the high pressure plasma from the coil-support/insulator assembly. This is the essence of centrifugal confinement as applied to fusion devices.

The centrifugal force constitutes an additional “knob” and is used to optimize magnetized plasma configurations. A configuration such as the one in Fig. 1 results in four advantages over tokamak-type devices.<sup>2</sup> The system is steady state, since all currents are externally driven. The system is free of disruptions, since there are no appreciable parallel currents and, consequently, no kink-type instabilities. There is a large velocity shear in the system which has the potential of stabilizing both micro- and macroinstabilities.<sup>3</sup> Microstabilization results in superior crossfield transport. Macrostabilization, in particular, stabilization of the interchange, flute mode, can lead to the very simple coil configuration such as in Fig. 1, the fourth advantage. A drawback of this system is that power is required to maintain the plasma rotation against viscous losses. On the other hand, we have shown elsewhere<sup>2,4</sup> that viscous heating could be sufficient to heat the plasma to fusion temperatures; therefore, no auxiliary heating power might be necessary (these conclusions were arrived at in Refs. 2 and 4 assuming that the heat and mo-

mentum losses were classical, an optimistic assumption). Another drawback is that the plasma beta is limited by the requirement on the sonic and Alfvén Mach numbers (supersonic and subAlfvénic). The electric field in the system has a threefold role: it ionizes and forms the plasma, it rotates and thereby contains the plasma, and it heats the plasma.

In this paper, we present a two-dimensional (2D) numerical study of the system depicted in Fig. 1. The numerical code is capable of simulating both MHD equilibrium as well as simple transport.<sup>5</sup> Since it is 2D, it is not set up to do a stability study; however, some of this latter work has been reported elsewhere and is ongoing.<sup>6</sup> Our objective in this paper is to demonstrate numerically that one can achieve centrifugal confinement—in the sense of detaching the plasma from the insulator and supports—and that the viscous dissipation can heat the plasma resulting in reasonable steady state plasma profiles.

The numerical code solves the magnetohydrodynamic (MHD) equations including transport from heat conduction, resistive diffusion, and viscosity. In addition to the above objectives, we have also been able to study penetration of the electric field during the formation of the confined plasma, and to test the 2D stability of the scheme. Our ancillary objective was to develop the capability of numerically simulating supersonically rotating plasma in the presence of insulating surfaces and biased electrodes.

In the next section we describe the equations, the numerical algorithm, and the boundary conditions used in the simulation. In Sec. III we describe the early-time formation of the plasma. In Sec. IV we analyze the steady state solution. In Sec. V we discuss a zero-dimensional model for momentum and heat balance. In Sec. VI, we present some parameter scans. We conclude in Sec. VII.

## II. NUMERICAL METHOD

We solve the time-dependent MHD and transport equations in the  $(R, z)$  plane of an  $(R, z, \phi)$  cylindrical coordinate system. Azimuthal symmetry is assumed. The governing equations for the density  $n$ , poloidal flow  $\mathbf{u}_\perp = (u_r, u_z)$ , tor-

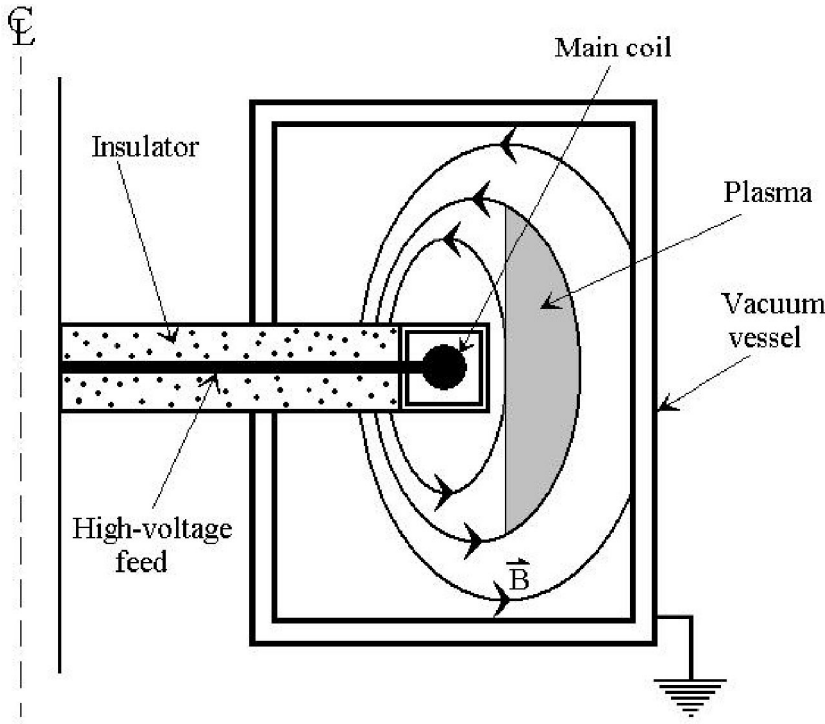


FIG. 1. Schematic of a one-coil magnetic configuration for a centrifugally confined plasma.

oidal flow  $u_\phi$ , toroidal magnetic field  $B_\phi$ , poloidal magnetic flux  $\psi$ , and temperature  $T$  are

$$\partial_t n + \nabla \cdot (\mathbf{u}n) = 0, \quad (1)$$

$$\begin{aligned} \partial_t (nMu_R) + \nabla \cdot (\mathbf{u}nMu_R) \\ = -\partial_R(2nT) - \frac{1}{R^2} \partial_R \left( \frac{1}{2} R^2 B_\phi^2 \right) - \frac{1}{R} J_\phi \partial_R \psi \\ + \frac{1}{R} nMu_\phi^2 + \nabla \cdot (nM\mu \nabla u_R), \end{aligned} \quad (2)$$

$$\begin{aligned} \partial_t (nMu_z) + \nabla \cdot (\mathbf{u}nMu_z) \\ = -\partial_z(2nT) - \frac{1}{R^2} \partial_z \left( \frac{1}{2} R^2 B_\phi^2 \right) \\ - \frac{1}{R} J_\phi \partial_z \psi + \nabla \cdot (nM\mu \nabla u_z), \end{aligned} \quad (3)$$

$$\begin{aligned} \partial_t (nMRu_\phi) + \nabla \cdot (\mathbf{u}nMRu_\phi) = \mathbf{B} \cdot \nabla (RB_\phi) + \nabla \\ \cdot (nM\mu R^2 \nabla (u_\phi/R)), \end{aligned} \quad (4)$$

$$\partial_t \left( \frac{B_\phi}{R} \right) + \nabla \cdot \left( \mathbf{u} \frac{B_\phi}{R} \right) = \mathbf{B} \cdot \nabla \left( \frac{u_\phi}{R} \right) + \eta \nabla \cdot \left( \frac{1}{R^2} \nabla (RB_\phi) \right), \quad (5)$$

$$\partial_t \psi + \mathbf{u} \cdot \nabla \psi = \eta R J_\phi, \quad (6)$$

$$\partial_t T + \nabla \cdot (\mathbf{u}T) = \frac{1}{3} T \nabla \cdot \mathbf{u} + \nabla_{\parallel} (\chi_{\parallel} \nabla_{\parallel} T) + \nabla \cdot (\chi_{\perp} \nabla T) + H, \quad (7)$$

where

$$\mathbf{B} = RB_\phi \nabla \phi + \nabla \phi \times \nabla \psi, \quad (8)$$

$$J_\phi = R \nabla \cdot \left( \frac{1}{R^2} \nabla \psi \right), \quad (9)$$

$$H = (2/3) M \mu R^2 |\nabla (u_\phi/R)|^2. \quad (10)$$

These are the one-fluid MHD Braginskii<sup>7</sup> equations with several simplifications as follows. The ion and electron temperatures are assumed equal. The simplest forms are used for the viscosity,  $\mu$ , for  $u_R$  and  $u_z$ . The form for the viscous force for  $u_\phi$  is calculated from Braginskii and ensures that the viscous force is zero if there is no gradient in the toroidal angular frequency of rotation,  $\Omega \equiv u_\phi/R$ . Simple isotropic resistivity,  $\eta$ , is used—note that it tends to relax the toroidal current  $J_\phi$  and tends to relax any toroidal field to its vacuum variation  $B_\phi \sim 1/R$ . The thermal diffusivity has an isotropic piece, proportional to  $\chi_{\perp}$ , and an added parallel thermal conduction, proportional to  $\chi_{\parallel}$ . Here,  $\nabla_{\parallel} \equiv (\mathbf{B}/B) \cdot \nabla$ . The term  $H$  is the viscous heating term, calculated from Braginskii with the simplification that only terms proportional to toroidal flow are kept—note that viscous heating is proportional to gradients in the toroidal angular frequency  $\Omega$ . We have also assumed that the resistive, Ohmic heating is small compared to the viscous heating; for centrifugally confined plasmas, this can be shown to be the case if classical transport coefficients are assumed. In the Appendix, we present a brief calculation that shows that resistive heating is small. For the purposes of this paper, we kept the dissipative coefficients  $\eta$ ,  $\chi$ , and  $\mu$  constant for the numerical simulation.

We apply the equations to the simulation box shown in Fig. 2. Figure 2 is an  $(R, z)$  cross section of the vacuum chamber. The lines in Fig. 2 are contours of  $\psi$  corresponding to the poloidal magnetic field lines. This field is produced by toroidal current in the coil placed in the middle of the box. Enveloping the coil and its support/feeds is a box as shown in the figure. The simulation volume for our system is between the inner and outer box. Appropriate boundary conditions are applied at these boundaries.

The boundary conditions are set up to mimic the outer wall as a good conductor. The inner box, however, is an insu-

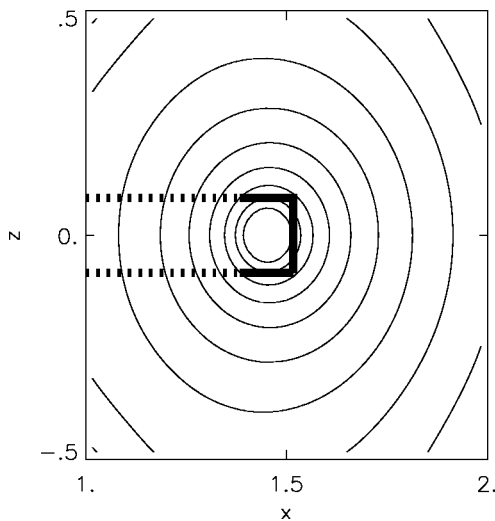


FIG. 2. The vacuum magnetic flux contours.

lator from  $R=1.0$  to  $R=1.4$ , shown in the figure by dotted lines; the remaining box is a conductor, shown as a bold solid line. Given these, the boundary conditions are set as follows: The normal derivative of the density is set to zero at all the walls. The temperature is fixed at all the walls to a low value (see below). The flux function,  $\psi$ , is “frozen-in” wherever there is a conducting wall—we accomplish this by matching to the vacuum solution as a boundary condition. At the insulating wall, however, we allow  $\psi$  to “float” by simply extrapolating from the simulation volume. Both components of  $\mathbf{u}_\perp$  are set to zero at the walls, corresponding to hard-wall, no-slip boundary conditions. The assumption of no-slip boundary conditions where field lines intersect conducting walls can be shown to be valid by using the MHD Ohm’s law, for the perpendicular flows, and no flow into the wall, for the parallel flows. For  $u_\phi$ , no-slip is assumed at all the walls except at the insulator where we use zero normal derivative: the idea is that, at a conducting boundary, potential drops cannot be maintained between neighboring field lines, hence there is no electric field there and hence no toroidal flow; at an insulator, however, potential drops can be maintained and there can be an electric field across lines, translating to a toroidal flow. The presence of an insulator on the “open” field line is, of course, a crucial part of centrifugal confinement schemes. The boundary conditions for  $B_\phi$  are also special. At the conducting surfaces, the normal derivative is set to zero. At the insulator,  $B_\phi$  is set to a nonzero number: on the top insulator,  $B_\phi$  is set to  $+I_R/(2\pi R)$ ; on the bottom insulator  $B_\phi$  is set to  $-I_R/(2\pi R)$ . The reason for the jump in  $B_\phi$  is that there is a thin, constant radial current,  $I_R$ , into the electrode that keeps the electrode charged up against “leakage” currents from the plasma. This current produces a jump in  $RB_\phi$  across the insulator. (We discuss this in more detail later.)

In this paper, we report our results using units normalized to reference values as follows: (a) *lengths* are normalized to the box size  $L$ . Thus, in normalized units, the dimensions of our box are  $1\times 1$  units; (b) *magnetic field* is normalized to a reference field  $B_0$ . Likewise, *plasma density*

is normalized to a reference density  $n_0$ . If the ion mass of the plasma species is  $M$ , then *speeds* are normalized to the reference Alfvén speed  $V_{A0}=B_0/(4\pi n_0 M)^{1/2}$ . Energy density is normalized to the magnetic energy density; (c) *time* is normalized to the reference Alfvén time  $L/V_{A0}$ .

Our model also includes transport coefficients, albeit in very simple constant forms. In particular, we use an isotropic viscous diffusivity  $\mu$ , an isotropic resistive diffusivity  $\eta$ , and an anisotropic heat diffusivity,  $\chi_\parallel$  and  $\chi_\perp$ , diffusivity parallel and perpendicular to the field lines. In each case, these are normalized to the reference diffusivity constructed from  $L$  and  $V_{A0}$ , given by  $LV_{A0}$ . In addition to these constant dissipative coefficients in the plasma, we also included enhanced friction on the plasma flow very near the plasma-wall boundaries. This was done primarily for numerical stability reasons, but it is also realistic as, near the walls, plasmas are generally affected by strong ion-neutral charge-exchange friction.

In what follows, we describe the formation and steady state properties for a reference case. We then report the results of a parameter scan about this reference case.

### III. FORMATION

The simulation box, corresponding to the vacuum vessel, is of size  $1\times 1$  length units. The left-hand side of the vessel was placed at a radius of 1.0 units from the central axis. A toroidal current carrying ring is placed at a radius of  $R=1.45$  units from the axis. This ring creates a vacuum magnetic field which is the starting point of the simulation. The corresponding flux contours are shown in Fig. 2. The magnetic field strength at the  $z=0$  midplane initially ranged from  $B=2.4$  units at the inner electrode (discussed below) to 0.3 units at the right wall. The dashed line in Fig. 2 shows the location of an insulator boundary that envelopes current “feeds” to the main coil. There is also a conducting plate, serving as an electrode, partially enveloping the main coil. This is shown as a solid line in Fig. 2. Note that the vacuum vessel is electrically insulated from the high voltage feed and the inner electrode. The vacuum vessel is grounded. In the course of the “experiment” there is a leakage current from the inner plate to the vacuum vessel, due to plasma viscosity. To maintain the inner plate at high voltage, there will be a radial current,  $I_R$ , along the high voltage feed to the inner electrode. For our simulation, this current translates to a boundary condition on the toroidal magnetic field at the insulator, as discussed above.

To the above magnetic field system, we added a cold, static plasma with an initially uniform density of 1 density unit and a temperature of 0.0003 energy units. Thus, the initial  $\beta\equiv 2nT/B^2$  of the plasma evaluated for  $B=1$  is 0.06%. The walls were held at the temperature 0.0003 throughout the simulation.

Given this initial condition, a constant current  $I_R$  is now made to flow into the electrode. In the numerical algorithm, this corresponds to a boundary condition on  $B_\phi$ . Specifically, since  $2\pi R$  times the jump in  $B_\phi$  must be proportional to the constant radial current, we applied the boundary condition that at the insulator the jump in  $RB_\phi$  across the gap is

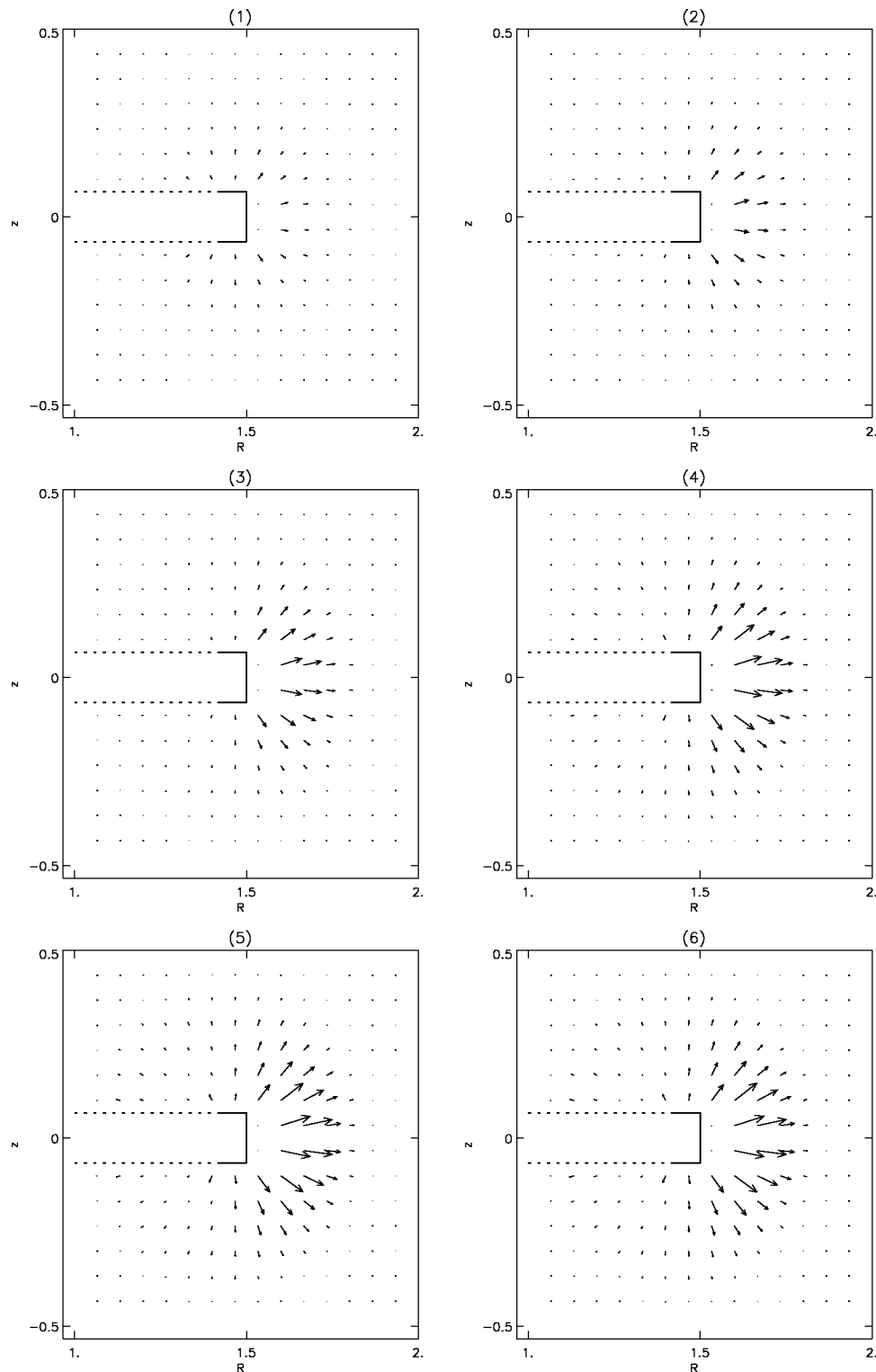


FIG. 3. Penetration of the electric field. The time scale over the five frames is approximately 400 Alfvén times.

fixed. For the parameters run in our experiment,  $RB_\phi$  ranged from 0.001 to 0.0085 units, much smaller than the main magnetic field. For our reference case,  $RB_\phi = 0.005$ ; this corresponded to a current  $I_R/I_0$  of 0.08, where  $I_0$  is the current in the main coil.

As a result of this current feed, the electrode becomes biased and an initial voltage drop is seen near the electrode. The associated electric field, which corresponds to plasma

toroidal rotation localized near the electrode, then starts to penetrate. For our simulation model, this penetration comes about as a result of crossfield viscous diffusion of the toroidal flow. The small toroidal component of the magnetic field near the plates also starts to penetrate. The net effect is a penetration of the electric field. We show the time sequence of this electric field penetration in Fig. 3.

For this run, we took the cross-field viscosity  $\mu$  and the

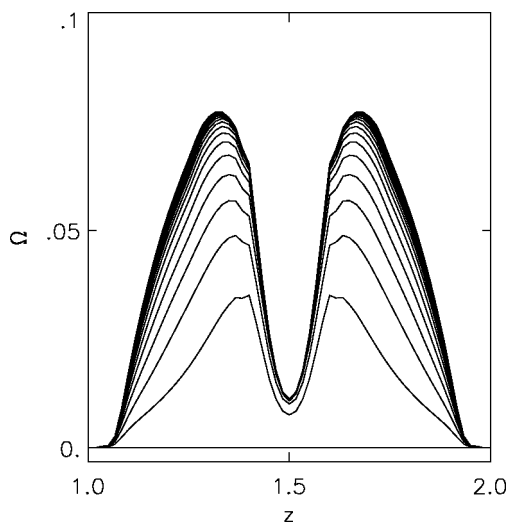


FIG. 4. Build-up and saturation of toroidal angular frequency of rotation. A cut along the  $z$ -axis at  $x=0.54$  is shown.

resistivity  $\eta$  to be equal. The resistivity  $\eta$  was taken to be 0.0005 units. These values correspond to a Lundquist number ( $RV_{A0}/\eta$ ) of about 3000. The observed time scale of the electric field penetration is consistent with the viscous time scale of about  $[(1/2)^2/0.0005]=400$  time units.

Figure 4 shows the build-up of the toroidal rotation in the plasma. Initially there is no rotation; however, when the  $B_\phi$  boundary condition at the insulators is applied, the plasma begins to rotate. The graph shows cuts, overlaid in time, of the angular frequency of rotation across the plasma. The cuts are taken vertically across the plasma at  $R=1.55$  units. The plasma cannot rotate near the inner electrode nor where the poloidal field cuts the vacuum vessel walls: these surfaces are conducting, freezing any cutting field lines. The rotation builds to a final steady-state as shown in the figure. In the steady state, the peak speed on the midplane is about 0.12 velocity units. This corresponds to a peak Alfvén Mach number of 0.23. This Mach number is large enough ( $M_s \sim 3.3$ ) that the poloidal field distends a bit, as was observed.

As the plasma rotation builds up, two things happen: the centrifugal forces build up, thus localizing the plasma pressure to the outboard side, and viscous heating sets in, raising the plasma temperature. The time sequence of the pressure build up is shown in Figs. 5 and 6. Figure 5 shows contour plots of the pressure with time (the last frame is shown in the gray scale to differentiate high pressure regions from low pressure; white denotes high pressure). Figure 6(a) shows a cut in the pressure across the  $z=0$  midplane at times corresponding to those in the contour plots. Figure 6(b) is a similar cut made just below the insulating brace shown in Fig. 2. Initially, the pressure is almost uniform, but this changes dramatically with time as the centrifugal forces extract pressure from around the insulator. In the steady state, for the reference case, the pressure drop from the peak to the insulator reached a factor of 40.

The time sequence of the density is shown in Fig. 7. The density behaved in a manner that was not expected. At first, centrifugal forces from the spinning plasma cause the density

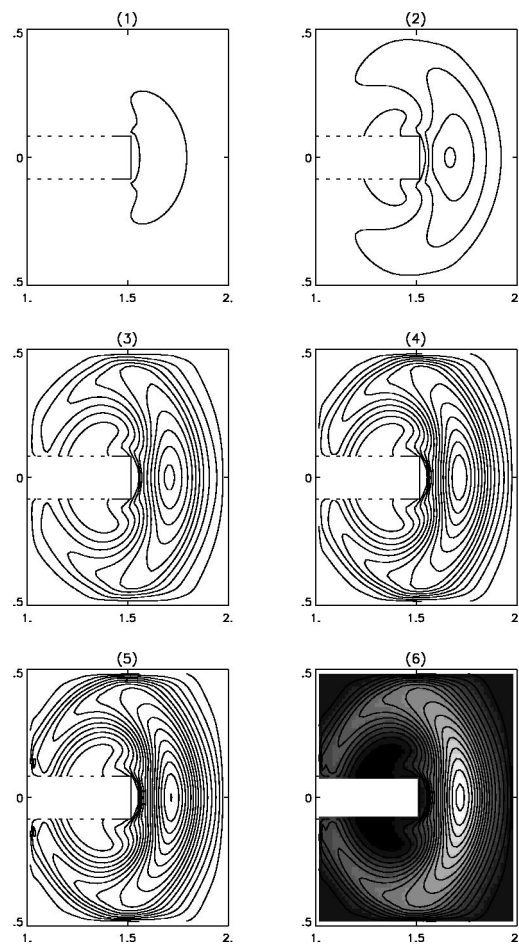


FIG. 5. Plasma pressure slings to the outboard side as rotation builds up. Same time scale as Fig. 3 (400 Alfvén times).

to pile up on the outward side. This pile up, however, is mitigated when viscous heating sets in: as the plasma heats up near this peak, it expels some density since a given centrifugal force contains pressure as a whole. The effect is to push some of the plasma back around to the inward side of the vacuum vessel while still maintaining the pressure drop. The final steady-state has three density peaks and two density troughs. These are evident in Fig. 7, especially in the last frame shown in gray scale. The trough is effectively zero-density while the peaks are all of about equal magnitude: about 2.5 times the original flat density. Note that the inverted density peaks are at the outer radii where  $\Omega \rightarrow 0$  and centrifugal forces are weak.

The details of the steady state transport equilibrium are described in the next section.

#### IV. STEADY STATE

After about 600 time units from the onset of the radial current feed, the system comes to a steady state. The applied voltage to the electrode causes a potential drop across the plasma. This drop, initially localized near the electrode, has now spread throughout the plasma on account of viscous coupling. There is thus an  $\mathbf{E}$  field across the plasma and a corresponding toroidal rotation. This rotation is subject to viscous losses since the boundary conditions at the wall are

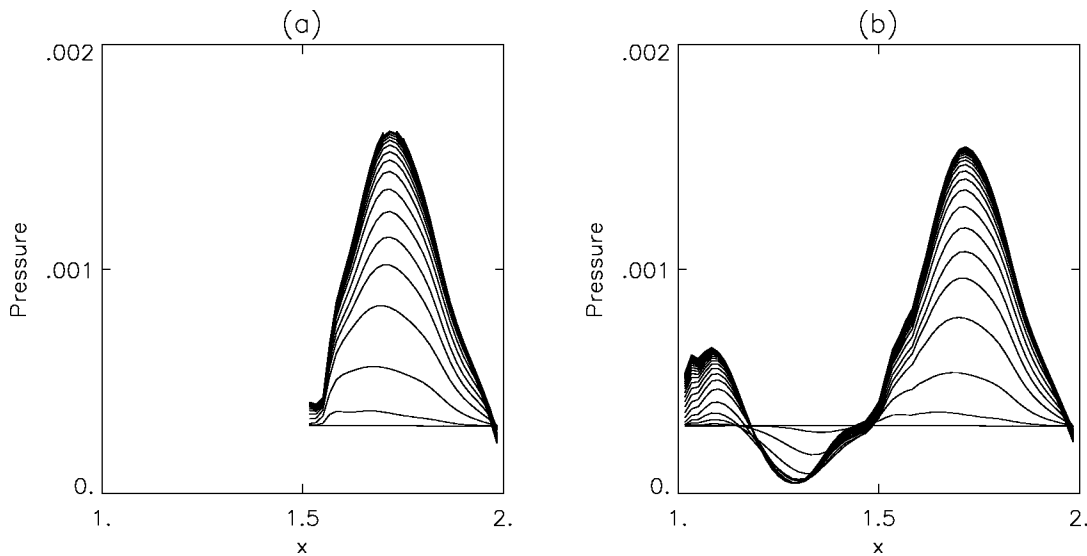


FIG. 6. Time sequence of pressure profile cut in  $x$ : (a) cut at the  $z$ -midplane; (b) cut immediately below the insulator.

no-slip. A radial current, from viscous “ $\mathbf{F} \times \mathbf{B}$ ” drifts, tends to neutralize the potential difference between the inner electrode and the vacuum vessel. To maintain the voltage, the radial current is supplied. In steady state, there is charge and voltage maintenance. Another way to look at this is that the

viscosity decelerates the plasma while the  $I_{\text{radial}} \times B_{\text{poloidal}}$  force tends to accelerate the plasma, resulting in steady state rotation.<sup>8</sup>

The plasma pressure localizes to the outboard side. The equation describing this localization is given in Refs. 1 and 2 by

$$\mathbf{B} \cdot \nabla p = -nM\mathbf{u} \cdot \nabla \mathbf{u}. \tag{11}$$

In the isothermal limit, this equation yields the solution

$$p(R, \psi) = p_0(\psi) \exp[MR^2\Omega^2/4T], \tag{12}$$

where  $p_0(\psi)$  is the pressure loading per flux surface, determined by crossfield transport. Note that the pressure drop is exponential and scales as  $\exp[M_s^2/4]$ .

In Fig. 8, we show contour plots of various quantities of interest in steady state. Figure 8(a) shows an angular frequency of the rotation in steady state. The rotation frequency is almost constant along flux surfaces, as expected from the theory: each flux surface rotates as a rigid rotor. Note, as discussed earlier, that field lines that terminate in conducting walls are line-tied and, thus, since  $\Omega = \Omega(\psi)$ , the plasma on that entire surface should not rotate. This effect is produced faithfully by the code—the plasma is not seen to rotate outside the “last good flux surface (LGFS).” An overlay of Figs. 8(a) and 2 confirms this. This phenomenon is also fairly well demonstrated for the field lines intersecting the brace—a blow-up of the contours close to the brace shows that frozen-in and line-tying seem to be working as expected, within the limits of the resolution of the code.

Figure 8(b) shows contours of pressure. Note that pressure is highly localized to the outboard side, consistent with Eq. (12).

Figure 8(c) shows contours of temperature. The temperature is at its highest near the outer wall because this is where the shear in the plasma rotation is the largest and viscous heating is maximum at maximum velocity shear. On the inboard side, towards the brace, there is also a local peak in the viscous heating rate since the velocity shear gets large here

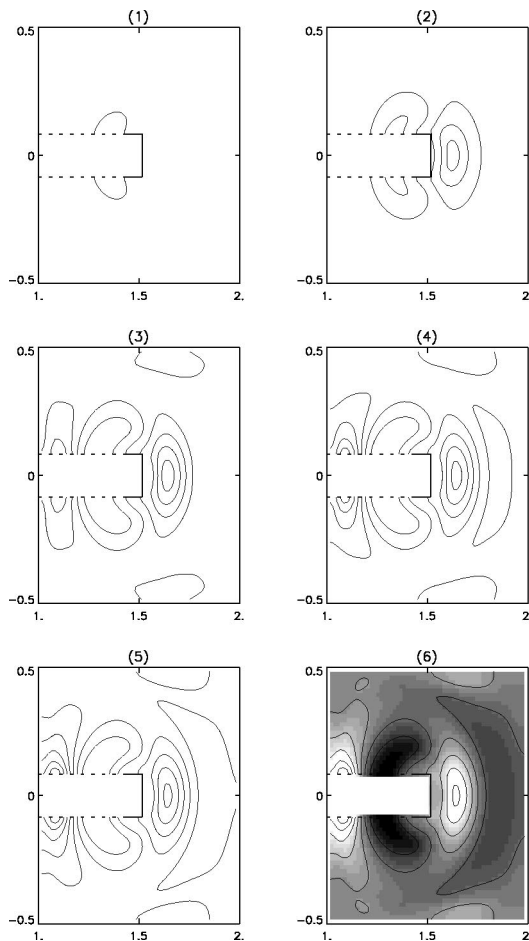


FIG. 7. Density contours corresponding to Fig. 5.

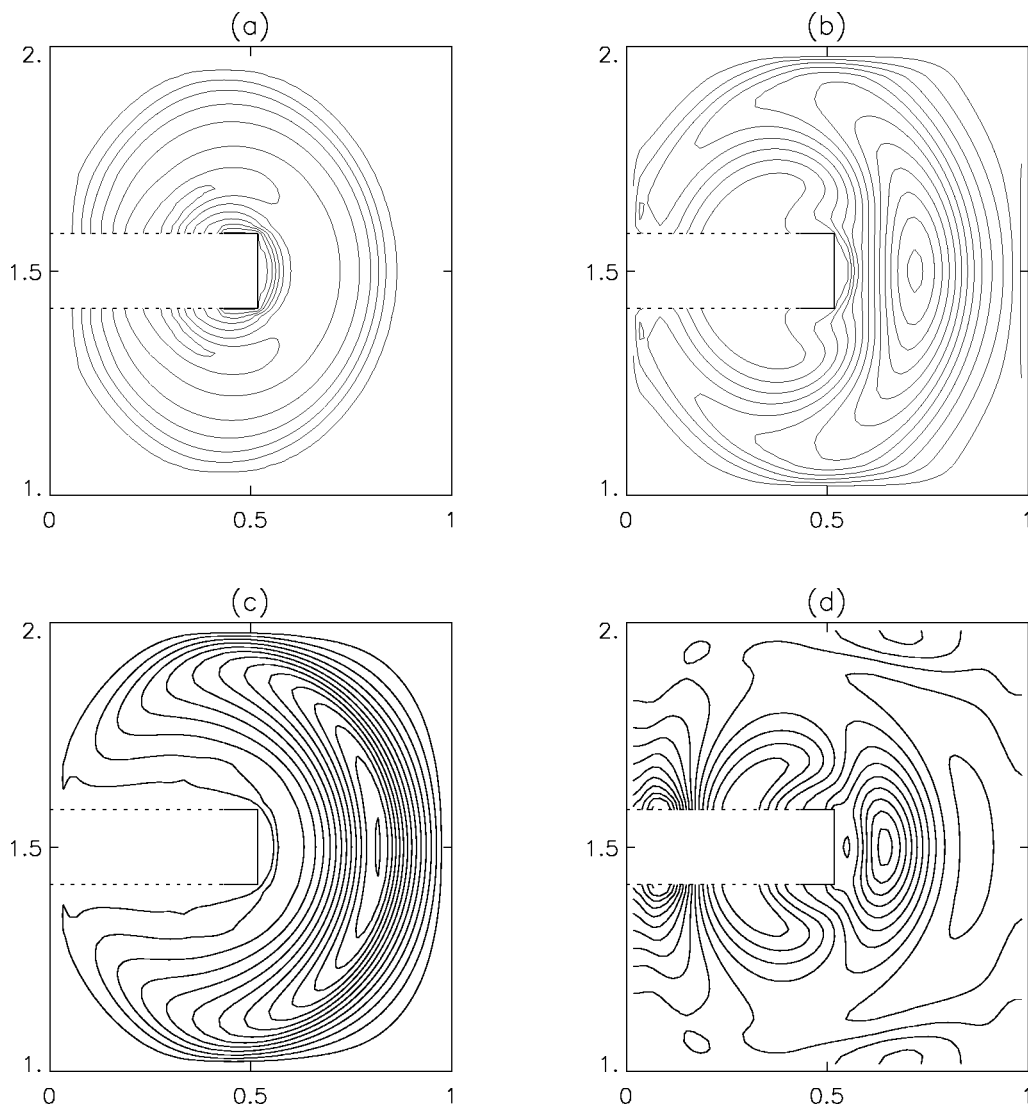


FIG. 8. Steady state contours. (a) Angular frequency relaxes to a flux function. Each magnetic surface thus rotates rigidly. (b) Pressure is highly localized to the outboard side. (c) Temperature contours: the profile is somewhat hollow since viscous heating maximises where the rotation shear is largest. (d) Density is localized to the outboard side; however, temperature profile effects also result in inboard density peaks.

too. Thus, we might expect the temperature profile to exhibit two peaks, at least in the transient phase, and a flat profile at the center in the steady state. We have indeed observed a subdominant inward peak in the temperature in the transient phase, in some cases. However, this peak is always overpowered by the outer peak. There could be three reasons for this: geometric effects, more effective thermal conduction to the brace because of closer proximity to it, relatively low numerical resolution closer to the brace. We have not differentiated these further. We note also that the temperature contours tend towards matching the flux contours. This is due to the relatively large parallel thermal conductivity. For this case, we used  $\chi_{\parallel}/\chi_{\perp} = 11$ .

In Fig. 8(d) we show density contours. As noted, the steady-state density is characterized by two troughs and three peaks.

In the steady state, the system exhibits a low level convection in the  $(R, z)$  plane. In Fig. 9, we show flow vectors of the steady state convection. It is important to note that the

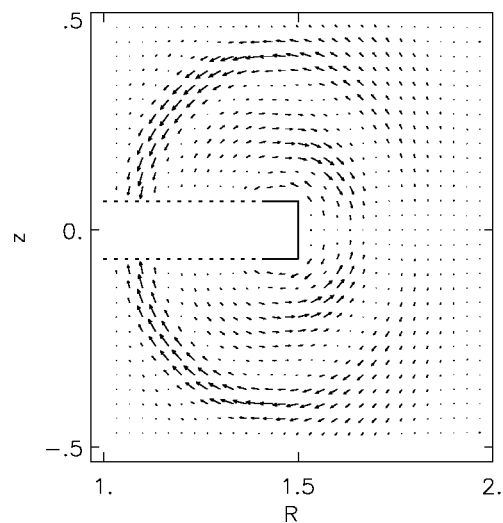


FIG. 9. Transport steady state is accompanied by low speed convection cells.

size of this flow is substantially smaller than the toroidal flow—for the case shown, the peak convective flow speed compared to the peak toroidal rotation speed was a factor of 1/875. The cell speeds scale as the inverse of the Reynolds numbers. These convection cells are the ubiquitous cells that one always observes in nonuniformly heated stratified equilibria.<sup>9</sup> The cells speeds are proportional to the resistivity. In this paper, we have assumed constant resistivity—this would have to be refined to include the temperature dependence of the resistivity if a quantitatively accurate flow pattern is desired.

## V. MOMENTUM AND HEAT BALANCE

In steady state, there is a balance between viscous momentum losses and the external  $I_R \times B$  forces. An equation expressing this is obtained by integrating Eq. (4) over the volume wherein the plasma rotates. This volume is bounded by those outermost flux surfaces that are free to rotate (see Fig. 1: field lines that terminate on conducting surfaces should be line-tied and not rotate) and by the insulator that envelops the high voltage feed (dashed line). (Hereafter, we will denote the outermost rotating flux surfaces as LGFS, “last good flux surfaces.”) When Eq. (4) is integrated over this volume, each term converts to a surface integral (by Gauss’ theorem) over the bounding surfaces just described. In that case, the  $d\mathbf{S} \cdot \mathbf{u}$  term vanishes over all the bounding surfaces, and the term  $d\mathbf{S} \cdot \mathbf{B}$  vanishes on the LGFS (by definition) but is nonzero on the insulator. For the viscous term, since  $\Omega = \Omega(\psi)$ ,  $d\mathbf{S} \cdot \nabla \Omega$  vanishes at the insulator but is nonzero over the LGFS. The resulting equation is

$$\int_{\text{LGFS}} d\mathbf{S} \cdot (\nabla \Omega) n M \mu R^2 = \int_{\text{insulator}} d\mathbf{S} \cdot \mathbf{B} R B_\phi. \quad (13)$$

The term on the right-hand side represents the discontinuity in  $B_\phi$  at the radial current feed, as discussed earlier. In particular, we have the relationship  $2\pi R[B_\phi] = I_R$ . Using the latter, and evaluating the integrals for large aspect ratio as well as in a “zero-dimensional” approximation, we have a 0D momentum balance equation,

$$NM(\mu/a^2)u_\phi = I_R BL, \quad (14)$$

where  $N = n \times (\text{Volume})$ . We have used  $L$  to estimate length scales of the various profiles and set all form factors to unity. The right-hand side represents the external  $j \times B$  force on the plasma, the left-hand side the resisting viscous forces.

In a like manner, a 0D equation for heat energy balance can be obtained from a volume average of Eq. (7). In doing so, the terms proportional to the flow  $\mathbf{u}$  vanish on the LGFS. The  $\chi_{\parallel}$  term is nonzero only on the insulator, i.e., there are electron heat losses at the insulator by parallel conduction along the field. The  $\chi_{\perp}$  term represents cross-field losses. The resulting equation is

$$\int_{\text{insulator}} d\mathbf{S} \cdot (\nabla (3/2)T)\chi_{\parallel} + \int_{\text{LGFS}} d\mathbf{S} \cdot (\nabla (3/2)T)\chi_{\perp} = \int_{\text{volume}} d\tau M \mu R^2 (d\Omega/dr)^2. \quad (15)$$

Using a large aspect ratio expansion and a zero-dimensional approximation, we may simplify this equation as we did the momentum equation above. The resulting 0D momentum and heat balance equations can then be written

$$NMu_\phi^2/\tau_{\text{mom}} = P_{\text{in}}, \quad (16)$$

$$(3/2)NT[1/\tau_{\perp} + 1/\tau_{\parallel}] = P_{\text{in}}, \quad (17)$$

where we multiplied the momentum balance equation (4) by  $u_\phi$  and defined the input power  $P_{\text{in}} \equiv I_R B a u_\phi$ . The various time scales are defined as

$$\tau_{\text{mom}} = L^2/\mu, \quad \tau_{\perp} = L^2/\chi_{\perp}, \quad \tau_{\parallel} = L^2/\chi_{\parallel}. \quad (18)$$

From (17) and (18), one may deduce an expression for the Mach number  $M_s$  by dividing the two equations into each other. We find<sup>2</sup>

$$M_s^2 = \frac{3}{2} \tau_{\text{mom}} \left[ \frac{1}{\tau_{\perp}} + \frac{1}{\tau_{\parallel}} \right] = \frac{3}{2} \left[ \frac{\chi_{\perp}}{\mu_{\perp}} + \frac{\chi_{\parallel}}{\mu_{\parallel}} \right]. \quad (19)$$

In classical collisional theory,  $\chi_{\perp}$  and  $\mu_{\perp}$  are of the same order. Thus, the Mach number is always greater than unity, which is desirable for centrifugal confinement (parallel heat losses add to the net heat loss while parallel momentum losses are smaller). For the purposes of this code, we have assumed collisional conditions (short mean free paths) to hold, thus the Braginskii expressions for thermal conduction, etc., are used. Fusion plasmas are collisionless; thus, collisionless transport must be used in more realistic models.<sup>10</sup>

## VI. PARAMETER SCANS

Starting from the baseline case reported above, we now changed parameters to assess the change in the equilibrium conditions as a function of various inputs.

From (16) and (17), we note that there is only one key input parameter, namely, the input power  $P_{\text{in}}$  or, equivalently, the radial current  $I_R$  supplied to the electrode. As  $I_R$  increases, we expect the rotation speed to increase. Figure 10(a) shows that as the current is increased, the angular frequency of plasma rotation also increases; on the abscissa, we plot the peak Alfvén Mach number; on the ordinate, we plot  $I_R/I_0$ , the radial current normalized to the current in the coil. As the rotation increases, the viscous heating increases, thus raising the temperature. This is shown in Fig. 10(b), where we plot the maximum temperature normalized to the wall temperature. Since both rotation speed and temperature go up with applied force, the Mach number must not go up as fast as the rotation. This is shown in Fig. 10(c). Finally, in Fig. 10(d), we show the maximum pressure drop as a function of the radial current.

## VII. SUMMARY

A 2D simulation has been run to investigate some key features of centrifugal confinement of magnetized plasmas for fusion. In this paper, we have studied the simplest possible such system: a single coil system. In a single coil system, a current-carrying ring creates a dipolar-type field. The ring is electrostatically biased with respect to the vacuum vessel, thus setting up a radial electric field and causing the

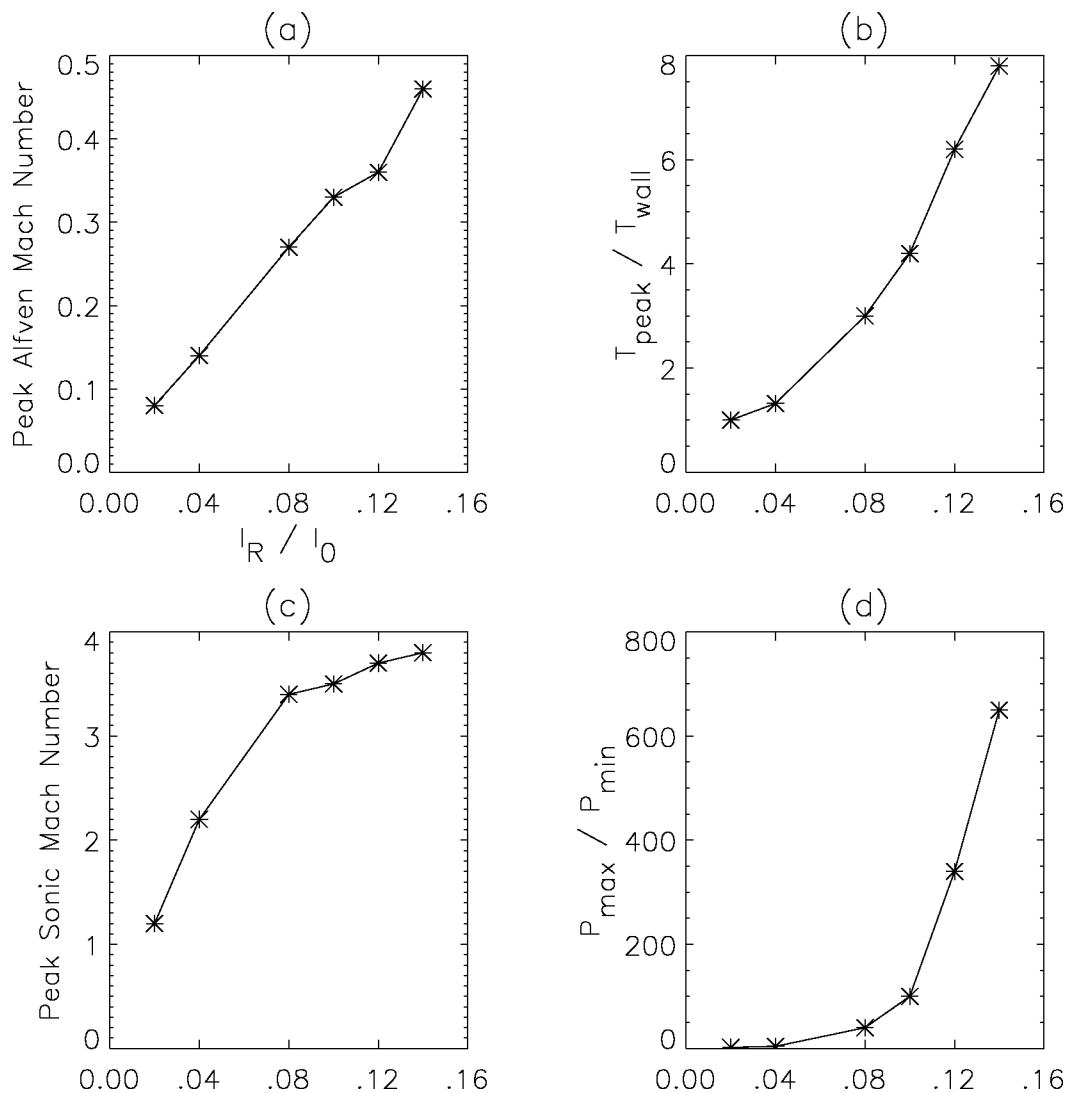


FIG. 10. Variation of various plasma parameters with increasing externally applied current,  $I_R$ .  $I_0$  is the current in the toroidal coil. Shown are (a) the peak Alfvén Mach number, (b) the peak temperature normalized to the wall temperature, (c) peak sonic Mach number, (d) ratio of the maximum to minimum pressures.

plasma to rotate toroidally. The resulting outward centrifugal forces sling the plasma towards the outer midplane. (In this sense, the system is not unlike the Io plasma torus of Jupiter, wherein the plasma is held in a torus due to centrifugal forces owing to the rotation of Jupiter.<sup>11</sup>) Since the plasma is now pulled away from the inner midplane, the toroidal current ring can be physically supported. Elsewhere, we have reported on similar 2D simulations done for a two-current-ring, magnetic mirror-like configuration.<sup>6</sup>

The central feature of centrifugal confinement—the slinging outwards of the plasma, detaching it from the supports on the inner midplane—has been confirmed by our numerical simulation in this paper. We have achieved a maximum pressure ratio,  $p_{\text{max}}/p_{\text{min}}$ , of about 650. This is not a physical limit on the system but a limit on the numerical performance of the code: where the density becomes small, the Alfvén speed rises putting severe restrictions on the time step from the Courant–Friedrichs–Levy condition. Work is in progress to address this limitation. The other central feature of centrifugally confined plasmas is that the temperature

can be made to rise simply from viscous heating alone. Our code has both resistivity and viscosity; thus, the plasma equilibrium we achieve is relaxed also with respect to transport. In our simulations, the Reynolds numbers are in the vicinity of 3000. We have shown that viscous heating indeed heats the plasma and that we achieved a maximum plasma  $\beta$  of order 3%. The maximum temperature ratio we achieve,  $T_{\text{max}}/T_{\text{wall}}$ , is about 8. Elsewhere, we have shown that this scenario can scale to a fusion reactor.<sup>2,4</sup>

There were some interesting unanticipated aspects that emerged from this simulation. We found that the density profile can have peaks in unexpected places. This is a result of the interplay between centrifugal confinement and heat sources: on nonrotating field lines, pressure tends to a constant, but these are near the maximum heat source locations, namely, where the rotation shear maximises. We also observed very low-level convection cells. This phenomenon is well-known, a consequence of the incompatibility between heating profiles, transport, and equilibrium force balance.

## APPENDIX: VISCOUS HEATING AND RESISTIVE HEATING

In this paper, we have assumed that viscous heating is the dominant heating source for the plasma particles. In particular, we ignore resistive heating. We show in this Appendix that it is reasonable to assume that resistive heating is smaller than viscous heating, at least if we use Braginskii transport coefficients.

The volumetric resistive heating rate is given by  $\eta j^2$ , where  $\eta$  is the Spitzer resistivity. The current is largely perpendicular to the magnetic field and can be obtained from the force balance equation,

$$nM\mathbf{u} \cdot \nabla \mathbf{u} = -\nabla p + \mathbf{j} \times \mathbf{B} + \nabla \cdot (nM\mu \nabla \mathbf{u}). \quad (\text{A1})$$

Solving for  $j_{\perp}$ , we find

$$\mathbf{j}_{\perp} = \mathbf{B} \times [nM\mathbf{u} \cdot \nabla \mathbf{u} + \nabla p - \nabla \cdot (nM\mu \nabla \mathbf{u})] / B^2. \quad (\text{A2})$$

The inertial term on the right-hand side is the largest of the three: it is larger than the pressure term by  $M_s^2$ , and larger than the viscous term by the Reynolds number  $au_{\phi}/\mu$ . Since  $\mathbf{u} \cdot \nabla \mathbf{u} \approx u_{\phi}^2 \hat{R}/R$ , we have

$$|j_{\perp}| < |u_{\phi}^2 / (RB)|. \quad (\text{A3})$$

We now compare the resistive heating rate to the viscous heating rate. This is the ratio

$$\eta j^2 : nM\mu R^2 |\nabla(u_{\phi}/R)|^2, \quad (\text{A4})$$

where the viscous heating was defined in Eq (10). Inserting the estimate for  $j$  in the left-hand side above, we find the ratio to be

$$(u_{\phi}/V_A)^2 : (R/a)^2 (\mu/\eta). \quad (\text{A5})$$

The expressions for  $\eta$  and the coefficient of viscosity  $\mu$  are given by Braginskii. We need the ratio of the two diffusivities. Assuming that  $T_e = T_i$ , the ratio  $\eta/\mu$  can be found to be of the order  $(c_s/V_A)^2 (M/m)^{1/2}$ , where  $m$  is the electron mass. Inserting this into Eq. (A5) above, we find the ratio of the resistive to the viscous heating rates to be

$$M_s^2 : (R/a)^2 (M/m)^{1/2}. \quad (\text{A6})$$

For our purposes, the left-hand side is of order 25. The right-hand side is of order  $60(R/a)^2$  for a D-T plasma. Thus, viscous heating is likely to dominate. In the simulation here, we have let  $\eta = \mu$ . Our Alfvén Mach number in the simulation is not too large. These conditions effectively make the viscous rate dominant for the simulation also.

## ACKNOWLEDGMENT

This work was supported by the DOE.

- <sup>1</sup>B. Lehnert, Nucl. Fusion **11**, 485 (1971).
- <sup>2</sup>R. F. Ellis, A. B. Hassam, S. Messer, and B. R. Osborn, Phys. Plasmas **8**, 2057 (2001).
- <sup>3</sup>P. W. Terry, Rev. Mod. Phys. **72**, 109 (2000).
- <sup>4</sup>A. B. Hassam, Comments Plasma Phys. Controlled Fusion **18**, 275 (1997).
- <sup>5</sup>P. N. Guzdar, J. F. Drake, D. R. McCarthy, A. B. Hassam, and C. S. Liu, Phys. Fluids B **19**, 134 (1976).
- <sup>6</sup>Y.-M. Huang and A. B. Hassam, Phys. Rev. Lett. **87**, 235002 (2001).
- <sup>7</sup>S. I. Braginskii, *Review of Plasma Physics* (Consultants Bureau, New York, 1960), Vol. 1, p. 205.
- <sup>8</sup>D. J. Griffiths, *Introduction to Electrodynamics* (Prentice-Hall, Englewood Cliffs, 1999), p. 358.
- <sup>9</sup>J. R. Drake, J. R. Greenwood, G. A. Navratil, and R. S. Post, Phys. Fluids **20**, 148 (1977).
- <sup>10</sup>V. P. Pastukhov, Nucl. Fusion **14**, 3 (1974).
- <sup>11</sup>J. W. Belcher, in *The Low Energy Plasma in the Jovian Magnetosphere, Physics of the Jovian Magnetosphere*, edited by A. J. Dessler (Cambridge University Press, Cambridge, 1983).